physica status solidi b
www.pss-b.com

Evidence of Spin Reorientation from Γ_4 to Γ_2 and Sign Reversal Exchange Bias in $CeCrO_3$ Nanoparticles

*Manish Yadav, Lekshmi S Kumar, Keshav Kumar, Deepankar Das, Qiang Zhang, and Chandana Rath**

Herein, the temperature-dependent magnetic structure and sign reversal exchange bias in $CeCrO_3$ using magnetization data and time-of-flight neutron diffraction data which is given less attention among $RCrO_3$ are investigated. While nuclear structural analysis using Rietveld refinement exhibits distorted orthorhombic structure within *Pnma* space group, temperature dependence of the magnetic structure using neutron diffraction reveals possible spin configurations, namely, Γ_4, Γ_2, and Γ_1, within the temperature range of 6–300 K. Temperature-dependent magnetization shows compensation temperature, T_{comp}, at 58 K, spin reorientation temperature, T_{SR}, at 15 K along with a Neel temperature, T_N, at 260 K which is the outcome of the competition between canted antiferromagnetic ordering of Cr^{3+} ions and Ce^{3+} ions in $CeCrO_3$. Furthermore, the magnetization versus magnetic field (M vs H) measurements indicate transition of the Γ_4 spin structure to Γ_2 spin structure around T_{SR} which is further supported by reversible-to-irreversible changes observed in temperature-dependent M_{FCC} and M_{FCW}. Moreover, a temperature-driven sign reversal of exchange bias in $CeCrO_3$ is observed, resulting from the competition between antiferromagnetic coupling between chromium moment (M_{Cr}) and cerium moment (M_{Ce}) in these nanoparticles. This intriguing behavior holds significant potential for the development of thermally assisted magnetic random access memory.

1. Introduction

The compound containing rare earth, having localized f-electrons, exhibits interesting physics at low temperatures, especially when these moments interact with transition-metal moments of the 3d-block that shows ordering at high temperature. Magnetic distorted perovskites, such as orthomanganites[1,2] and orthoferrites,[3,4] are examples of promising compounds for magnetoelectric multiferroicity. The rare-earth orthochromites ($RCrO_3$) on the other hand are additionally intriguing because of their coexisting functionalities that include multiferroicity,[5–7] spin reorientation (SR),[8–18] and magnetization reversal, which present the possibility of innovative applications in switching devices[19–21] and magnetic refrigeration.[22] In $RCrO_3$, several magnetic interactions are possible, including Cr^{3+}–Cr^{3+}, Cr^{3+}–R^{3+}, and R^{3+}–R^{3+}. Each magnetic interaction comprises isotropic, symmetric, and antisymmetric anisotropic exchange interactions.[10,23–26] Just below Neel temperature (T_N), the Cr–Cr magnetic interaction is dominated. At the intermediate temperatures, Cr–R interactions become increasingly important while at very low temperatures, R–R interaction is dominated. The unique properties of these compounds stem from the polarization of R^{3+} moments under the influence of internal field of Cr^{3+} moments, due to the presence of antisymmetric superexchange and the underlying Dzyaloshinskii–Moriya (DM) interactions.[10,24] Magnetization reversal is one of the important phenomena characterized by the spontaneous change in sign of the magnetization at a compensation temperature (T_{comp}) under a low applied magnetic field. This behavior has been observed in a few types of materials, including ferrimagnetic,[27,28] canted antiferromagnetic (AFM),[11,12,15,17] and ferromagnetic (FM) materials.[29] In canted antiferromagnets like $RCrO_3$, magnetization reversal arises from the AFM coupling between the rare-earth and transition metal moments. This property is highly desirable for applications in magnetic storage and magnetic switches, offering potential opportunities in these fields.[17]

The other interesting effect is exchange bias (EB), which has garnered significant attention due to its wide range of useful applications in spin valves, data storage, and magnetic sensors. The EB effect is described by the displacement of hysteresis loops across the magnetic field or magnetization axes when the system undergoes cooling in the presence of a magnetic field. The initial discovery of EB has been made by Meiklejohn and Bean in slightly oxidized cobalt particles.[30] Typically, displacement of hysteresis loop along negative field axis indicates the negative EB (NEB). In contrast, displacement in positive field axis

M. Yadav, L. S. Kumar, K. Kumar, D. Das, C. Rath
School of Materials Science and Technology
Indian Institute of Technology (Banaras Hindu University)
Varanasi 221005, India
E-mail: crath.mst@iitbhu.ac.in

Q. Zhang
Neutron Scattering Division
Oak Ridge National Laboratory
Oak Ridge, TN 37831, USA

The ORCID identification number(s) for the author(s) of this article can be found under https://doi.org/10.1002/pssb.202400372.

DOI: 10.1002/pssb.202400372

demonstrates positive EB (PEB). It is widely acknowledged that the presence of FM coupling at the interface between FM and AFM materials is a crucial requirement for NEB whereas for PEB, an AFM coupling at the FM–AFM interface is necessary.[31]

Apart from these exciting phenomenon, SR is also a prominent feature of $RCrO_3$. Investigations on $RCrO_3$ have revealed that these orthochromites exhibit various kinds of field-driven SR, causing the subtle FM moment to align with the applied magnetic field direction. In $RCrO_3$, there are mainly three different spin structures, Γ_1 (A_x, G_y, C_z; C_z^R), *Pn'm'a*: Γ_2 (F_x, C_y, G_z; F_x^R, C_y^R), and *Pn'ma'*: Γ_4 (G_x, A_y, F_z; F_z^R) according to Bertaut's notation.[10,32–34] For nonmagnetic R ions, $RCrO_3$ demonstrates weak FM behavior in the Γ_4 configuration. On the other hand, in the case of magnetic R ions, while the magnetic structure at high temperature below T_N is Γ_4, at low temperatures, spin structure can be Γ_2 or Γ_1.[5,10] There are few $RCrO_3$ which shows negative magnetization (magnetization reversal), for example, $GdCrO_3$, $TmCrO_3$, $YbCrO_3$, and $CeCrO_3$.[35–39] In these systems, negative magnetization is well explained by AFM coupling between Cr^{3+} and R^{3+}. While $GdCrO_3$ exhibits a canted AFM ordering of Cr^{3+} of the Γ_4 type just below T_N, $YbCrO_3$ and $TmCrO_3$ show the Γ_2-type canted AFM ordering.[35–37] In the case of $GdCrO_3$, the SR of Cr^{3+} from the Γ_4 to Γ_2 type occurs as the temperature decreases below T_N.[35] However, $YbCrO_3$ and $TmCrO_3$ maintain the Γ_2 magnetic structure for Cr^{3+} even at low temperatures.[36,37] Among these $RCrO_3$ compounds, $CeCrO_3$ nanoparticles have not been given enough attention to understand the structure-dependent magnetic properties. Hence, we have attempted to confirm the magnetic structure using temperature-dependent neutron diffraction and complementing it with magnetic measurements.

Here, we have analyzed its nuclear and magnetic structure using X-ray diffraction (XRD) and neutron diffraction and shown the formation of a distorted orthorhombic *Pnma* structure. The magnetic structural analysis demonstrates no clear magnetic structure transition within 6–300 K. Along with neutron diffraction, various magnetic measurements provide evidence for a SR from Γ_4 to Γ_2 spin structure around T_{SR} in $CeCrO_3$. M versus H also shows the switching of EB from positive to negative which makes these materials a potential candidate for thermally assisted magnetic random access memory (TAMRAM).

2. Results and Discussion

2.1. Structural and Compositional Analysis

XRD and time-of-flight (TOF) neutron powder diffraction (NPD) techniques are employed to ascertain the nuclear and magnetic structure of $CeCrO_3$ nanoparticles respectively. **Figure 1**a displays the XRD pattern obtained at room temperature of $CeCrO_3$ with the Rietveld refinement using *Pnma* space group and pseudo-Voigt peak profile function. The best fit affirms the existence of a single-phase orthorhombic, *Pnma* structure. The refinement of TOF NPD pattern at room temperature is conducted using the "T.O.F. p-Voigt * B-t-B exponential" peak profile function. The results are shown in Figure 1b. NPD fitting

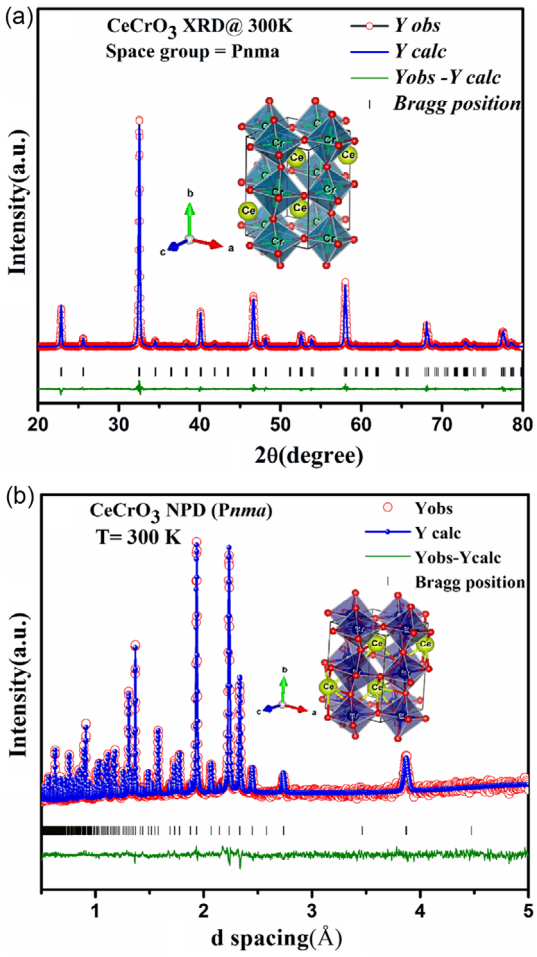

Figure 1. Rietveld refined room-temperature a) XRD and b) TOF NPD data of the same $CeCrO_3$ sample.

confirms that within *Pnma* structure, Ce, Cr, and the two oxygen atoms O1 and O2 occupy the 4c, 4b, 4c, and 8d Wyckoff positions, respectively. The structural parameters obtained from refinement are shown in **Table 1** and the crystal structure models generated from Crystallographic information file (CIF) after refinement are depicted in the corresponding insets of Figure 1a,b. The lattice parameters a, b, c, and the unit cell volume along with bond angle are closely matched with the previous report on $CeCrO_3$ synthesized through combustion method.[38–41] Apical Cr—O1 bond length and planner Cr—O2 and Cr—O2' are found to be unequal which confirms the octahedral distortion in $CeCrO_3$. There is a notable correspondence between the refined parameters obtained from our XRD and NPD patterns and the previously reported data and hence reliable to discuss further the temperature-dependent NPD. Scanning electron microscopy (SEM) image of $CeCrO_3$ perovskite synthesized through solution combustion method is shown in **Figure 2**a. The determined average particle size measures ≈50 nm. Energy-dispersive spectra (EDS) spectra show almost equal contribution of Ce and Cr as tabulated in the inset of Figure 2b.

Table 1. Crystal structure parameters of $CeCrO_3$ obtained from the Rietveld refinement RT and low-temperature (215 and 6 K) diffraction (XRD and TOF NPD) data.

Temperature data type	300 K XRD	300 K NPD	215 K NPD	6 K NPD
a	5.4743(3)	5.47377(17)	5.47077(18)	5.4686(3)
b	7.7340(3)	7.7314(2)	7.72453(17)	7.7134(2)
c	5.4802(3)	5.47925(19)	5.47604(16)	5.4742(2)
V	232.02	231.8813	231.4127	230.88
Ce				
x	0.0273(1)	0.0290(1)	0.0292(1)	0.0295(1)
y	0.25000	0.25	0.25	0.25
z	−0.0066(2)	−0.0062(3)	−0.0061(3)	−0.0064(2)
Cr/Fe				
x	0.00	0	0	0
y	0.00	0	0	0
z	0.50	0.5	0.5	0.5
O1				
x	0.4878(14)	0.4930(16)	0.4857(16)	0.4848(15)
y	0.25000	0.25	0.25	0.25
z	0.075(2)	0.075(3)	0.070(2)	0.072(2)
O2				
x	0.281(2)	0.280(3)	0.283(2)	0.286(2)
y	0.0333(14)	0.0325(14)	0.0372(12)	0.0347(12)
z	0.720(2)	0.712(2)	0.718(2)	0.719(2)
Cr(Fe)-O1-Cr(Fe)	155.69(9)	155.963	155.787	155.33
Cr(Fe)-O2-Cr(Fe)	159.5(5)	157.6	157.4	157.05
Cr(Fe)-O1	1.978(2)	1.9762(5)	1.9751(5)	1.9739(7)
Cr(Fe)-O2	1.971(11)	1.977(11)	1.9739(16)	1.977(2)
Cr(Fe)-O2'	1.964(11)	1.9707(11)	1.9729(16)	1.971(2)
<Cr-O>	1.971	1.9746	1.9740	1.9740

2.2. Neutron Diffraction

The TOF neutron diffraction data of $CeCrO_3$ at different temperatures ranging from 6 K to 300 K, are shown in **Figure 3**. The refinement of RT NPD pattern with *Pnma* space group shows that except (110)/(011), all additional peaks stem from coherent nuclear scattering of neutrons. The Neel temperature T_N is reported to be 260 K.[40,41] Below T_N, that is, at 215 K, a prominent magnetic scattering peak is observed at $d = 4.45$ Å. Such an additional Bragg peak confirms the long-range AFM ordering below T_N. Further, other magnetic contribution is noticed from the peaks at $d = 2.3$ and 1.7 Å corresponding to the Bragg peaks (211)/(031) and (310)/(231), respectively. The intensity of these peaks also increases with decrease in temperature. In literature, (110)/(011) and (211)/(031) are also observed by Taheri et al. and Shukla et al. in $CeCrO_3$.[38–41] In addition, Shukla et al. reported an additional Bragg peak below 100 K at $d = 3.15$ Å due to the polarization of Ce^{3+}.[38] However, we do not observe such peaks in NPD pattern below 100 K, as reported by Taheri et al.[41] The intensity of (110)/(011) is found to increase below 215 K, upto 61 K, and remains unaltered with further decrease in temperature. Further, we have carried out the nuclear refinement of the low-temperature neutron diffraction patterns to determine the size of the magnetic and chemical unit cell which is found to be same. The magnetic peaks are indexed as (110) and/or (011) based on the *Pnma* parent unit cell basis vector, the magnetic propagation vector, **k**, is (0,0,0). In the occurrence of various possible spin configurations for $\mathbf{k} = (0,0,0)$, the magnetic ordering for a *Pnma* structure is well studied and successfully applied on rare-earth orthochromites.[41] For $\mathbf{k} = (0,0,0)$ there are eight possible spin configurations of a *Pnma* structure with magnetic ions at 4b and 4c site, as shown in **Table 2**. From the eight possible irreducible representation (irreps), only four irreps such as Γ_1, Γ_2, Γ_3, and Γ_4 are allowed for the finite ordered moment of 4b site transition metal magnetic ion. The remaining four Γ_5, Γ_6, Γ_7, and Γ_8 are allowed at the 4c site for rare earth magnetic ion. The spin configurations of Cr^{3+} and Ce^{3+} magnetic ions are determined from comprehensive refinement of both nuclear and magnetic structures using Full-Prof. The Bilbao crystallography server is utilized for generating magnetic structure crystal information files (MCIFs) with desired superimposition of more than one irreps. For magnetic structure refinement, out of the eight possible spin configurations, only those that have a finite moment at the 4b site (Cr^{3+}) are selected, that is, *Pnma*: Γ_1 (A_x, G_y, C_z; C_z^R), *Pn'm'a*: Γ_2 (F_x, C_y, G_z; F_x^R, C_y^R), *Pnm'a'*: Γ_3 (C_x, F_y, A_z; C_x^R, F_y^R), and *Pn'ma'*: Γ_4 (G_x, A_y, F_z; F_z^R).[10] During refinement, all the components of the selected irreps are set free. Considering the contribution of Ce^{3+} along with the magnetic ion with Cr^{3+}, the fitting shows no significant improvement in goodness of fit parameters. Since rare earth ions show ordering at low temperature, it is quite unphysical to consider Ce^{3+} ordering at high temperature, that is, at 215 K. Therefore, the observed magnetic ordering totally arises due to Cr^{3+} only (Cr^{3+}–O–Cr^{3+}). Such magnetic ordering of Cr^{3+} below T_N is canted in nature and it gives rise to the weak FM moment due to D–M interaction.[10] The NPD data obtained at 215 K demonstrates a nearly identical fitting pattern with the magnetic structures Γ_4, Γ_2, and Γ_1 (**Figure 4**a–c). Similarly, at temperature 6 K, the NPD data also exhibits a comparable fitting pattern with the magnetic structures Γ_4, Γ_2, and Γ_1 (Figure 4d–f). Due to the minimal disparity in the lattice parameters, a and c, as well as the strong coupling between the magnetic moments along (110) and (011) directions, it becomes challenging to ascertain the exact magnetic configurations based solely on the fitting results. In literature, Shukla et al. reported Γ_4 magnetic structure in $CeCrO_3$ in the temperature range of 22–260 K excluding the additional Bragg peak below 100 K. It is well known that the magnetic structure transitions from Γ_4 to Γ_2 or Γ_1 in $RCrO_3$ with magnetic rare earth ions which occurs due to either the polarization of rare earth ions due to Cr^{3+} or due to weak rare earth ordering.[10] In this context, Cao et al. reported SR transition from Γ_4 to Γ_2 when temperature decreased from 16 K to 6 K. In this case, we have carried out few magnetic measurements to ascertain the Γ_4 to Γ_2 magnetic structural transition in these $CeCrO_3$ nanoparticles.

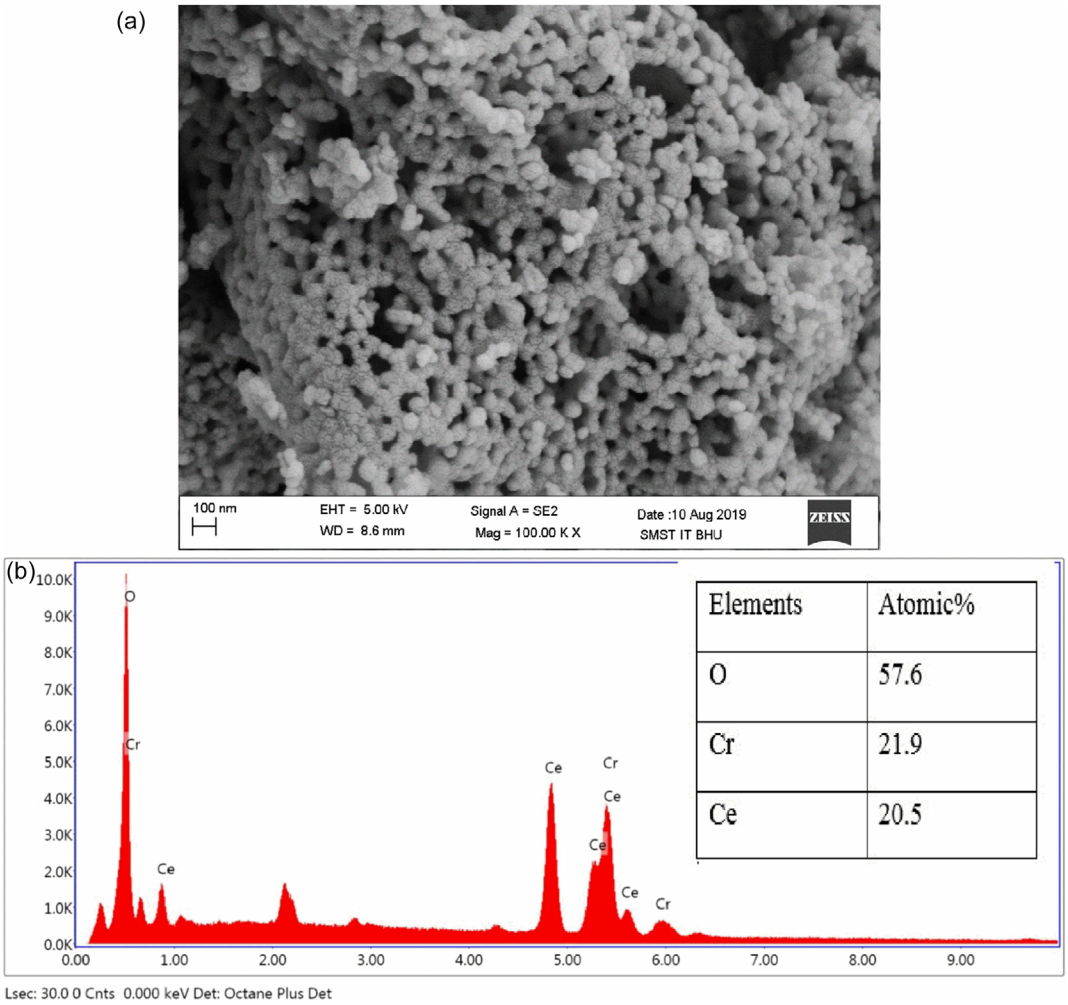

Elements	Atomic%
O	57.6
Cr	21.9
Ce	20.5

Figure 2. a) SEM micrograph and b) EDS spectra of $CeCrO_3$. (In EDS spectra, *X*-axis illustrates the energy in keV, while the *Y*-axis shows the intensity count).

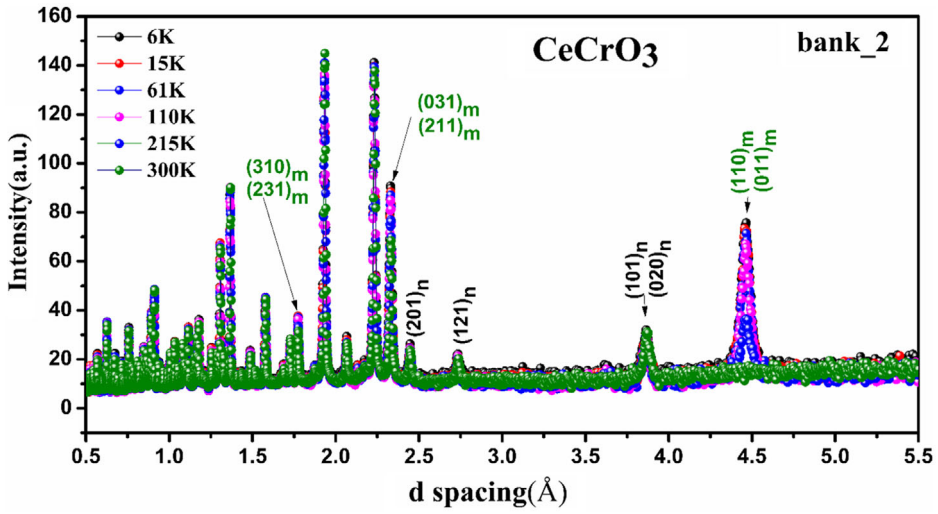

Figure 3. Temperature-dependent TOF-NPD data taken during warming at 6, 15, 61, 110, 215, and 300 K.

Table 2. The distinct irreducible representations (irreps) and their associated magnetic basis vectors for the moment arrangements of magnetic ions at positions (4b) and (4c) within a *Pnma* crystal structure, for the magnetic propagation vector $\mathbf{k} = (0,0,0)$.

Space group	irreps	4b (Cr)	4c (Ce)
Pnma	Γ_1	A_x, G_y, C_z	–, –, C_z^R
Pn'm'a	Γ_2	F_x, C_y, G_z	F_x^R, C_y^R, –
Pnm'a'	Γ_3	C_x, F_y, A_z	C_x^R, F_y^R, –
Pn'ma'	Γ_4	G_x, A_y, F_z	–, –, F_z^R
Pn'm'a'	Γ_5	–, –, –	G_x, A_y, –
Pnma'	Γ_6	–, –, –	–, –, A_z
Pnm'a	Γ_7	–, –, –	–, –, G_z
Pnm'a	Γ_8	–, –, –	A_x, G_y, –

2.3. Magnetization Studies

2.3.1. Magnetization versus Temperature

Temperature-dependent magnetization under ZFC (zero field cooled) and FCW (field cooled warming) of $CeCrO_3$ at 0.5 kOe external applied magnetic field is shown in **Figure 5**a. Magnetization curve recorded under ZFC and FCW mode shows a paramagnetic-to-AFM transition, T_N at 260 K, which is consistent with the T_N reported for both bulk and nanoparticles of $CeCrO_3$.[19,39–41] T_N is due to the ordering of Cr^{3+} moments at 260 K. Below T_N, field cooled magnetization (M_{FCW}) increases showing a maximum magnetization of ≈0.049 emu g^{-1} at ≈215 K (T_{max}). Such increase in magnetization arising due to the canted AFM ordering of Cr^{3+} moment results into a weak FM component in the field direction. Further with decrease in temperature, M_{FCW} decreases. The decrease in M_{FCW} is ascribed to the imposition of local internal field on Ce^{3+} moments generated from canted AFM ordering of Cr^{3+}. Therefore, the Ce^{3+} moments experience a resultant local field, which comprises the combination of applied external field and the internal field due to the Cr^{3+} moments. The resultant AFM coupling between Ce^{3+} and the canted Cr^{3+} moments polarizes the Ce^{3+} moments antiparallel to the weak FM component of the canted Cr^{3+} moment. With further decrease in the temperature, the competition between Cr^{3+} and Ce^{3+} moments results in the compensation of the net magnetization which is observed at 58 K, T_{comp}. Below T_{comp}, a negative magnetization is observed, which approaches a maximum magnitude of 0.056 emu g^{-1} at a

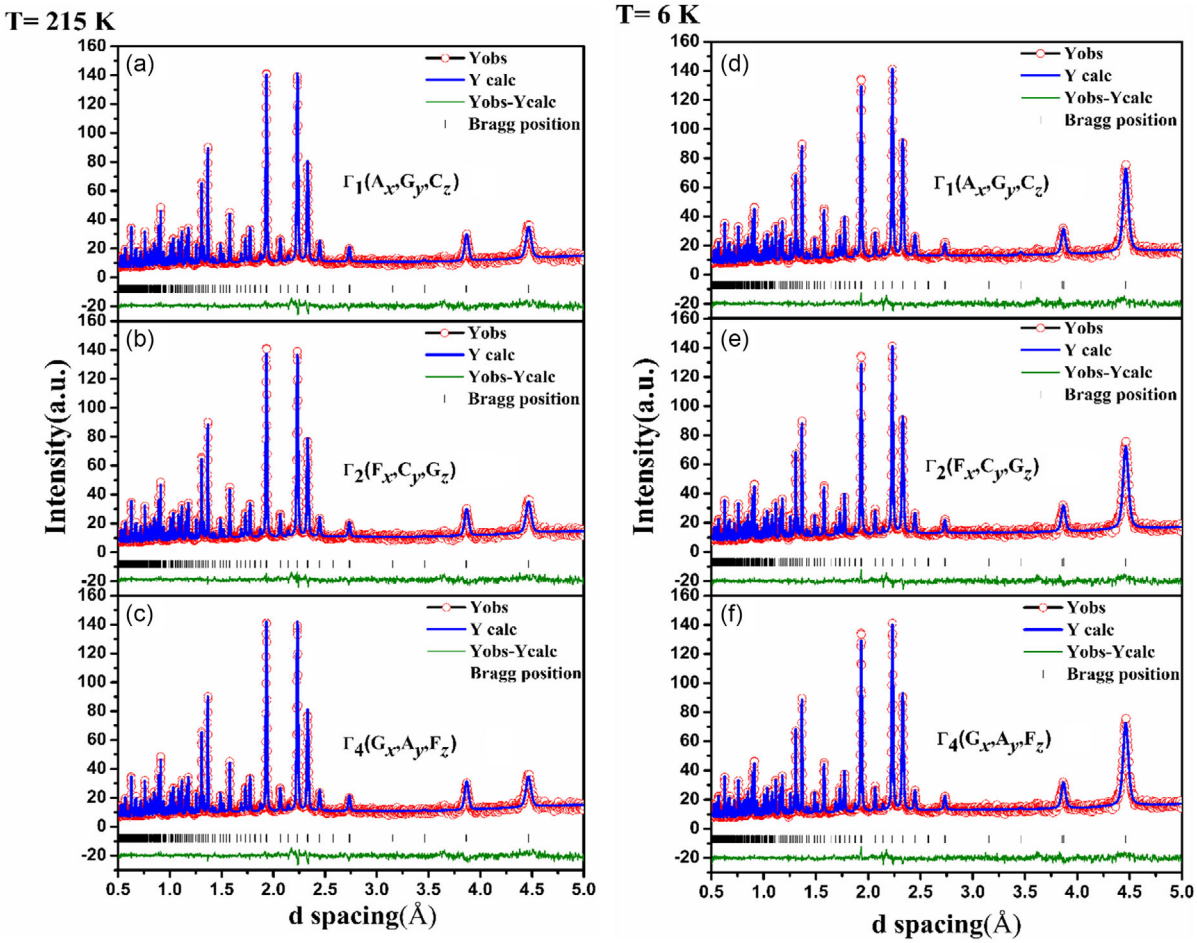

Figure 4. Rietveld refined TOF NPD patterns collected at a–c) 215 K and d–f) 6 K showing the typical fit quality of the refinement based on Γ_1, Γ_2, and Γ_4 irreps, respectively.

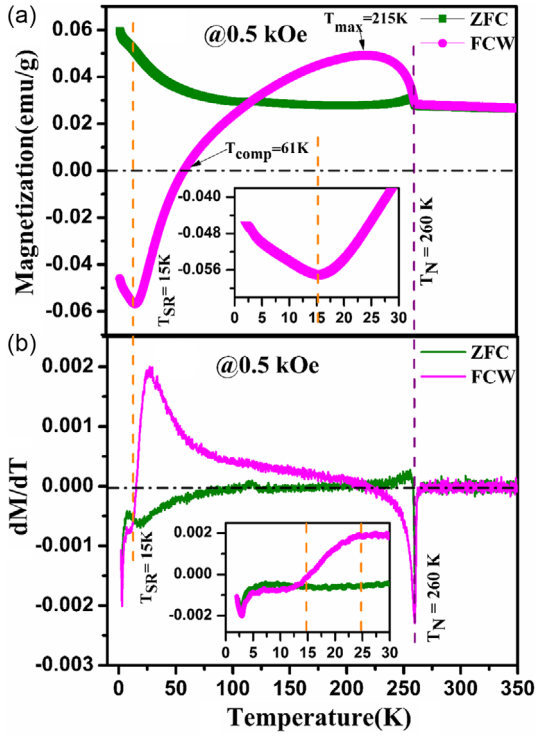

Figure 5. a) ZFC and FCW dc magnetization data of $CeCrO_3$ measured under 0.5 kOe. b) The corresponding first-derivative (dM/dT) curves.

temperature known as SR transition, T_{SR}, observed at 15 K followed by an increase in magnetization down to 2 K. Inset of Figure 5a depicts the enlarged view of T_{SR}. On the other hand, M_{ZFC} remains positive in the whole temperature range of 2–350 K. Below T_N, M_{ZFC} shows a maximum at 260 K and remains unchanged down to 110 K. Further with decrease in temperature, M_{ZFC} increases down to 2 K, followed by a change in slope at 20 K. Such change in slope corroborates with the T_{SR} and is attributed to the ordering of Ce^{3+} as reported previously.[19] Similar magnetization under ZFC has been observed in $GdCrO_3$ around T_{SR}.[35] The first derivative of M_{ZFC} and M_{FCW} versus temperature is shown in Figure 5b. Negative kink in dM/dT at 260 K further confirms the T_N. Below T_N, a maxima at 30 K in FCW accompanied by a minima in ZFC at 20 K is observed. Thereafter, at around 15 K, both the curves cross each other, indicating the rotation of Cr^{3+} moment to a new spin configuration between 30 and 15 K. A similar kind of rotation has been previously reported in $GdCrO_3$ and $SmCrO_3$.[35,42] The susceptibility of $CeCrO_3$ in ZFC, FCW, and FCC modes is found to be same as that of $GdCrO_3$, $TmCrO_3$, and $YbCrO_3$.[35–37] In these systems, negative magnetization is well explained by the rotation of rare earth moment in the internal magnetic field generated from the canted Cr^{3+} FM component. $GdCrO_3$ exhibits a canted AFM ordering of Cr^{3+} of the Γ_4 type just below T_N, which transforms to Γ_2-type AFM ordering at low temperature due to the rotation of Cr^{3+} in AC plane.[35] Similarly canted AFM ordering of Cr^{3+} has also been reported in $YbCrO_3$ and $TmCrO_3$.[36,37] Therefore, we believe that $CeCrO_3$ also exhibits a canted G_z-type AFM ordering of Cr^{3+}. For better understanding of change in spin configuration, we have performed a number of temperature-dependent magnetization measurements under FCC and FCW at 0.5 kOe external magnetic field. FCC/FCW magnetization versus temperature measurements carried out from 350 K down to 70, 45, 30, 15, 10 K are shown as **Figure 6**. It is evident from measurement that the temperature-dependent magnetization is reversible for 70, 45, and 30 K. However, the plot at 15 and 10 K shown as inset of Figure 6 clearly demonstrates the irreversibility in M_{FCC} and M_{FCW}. Below 30 K, that is, at 15 K, the M versus T becomes irreversible. While complete reversibility in FCC and FCW within temperature range 30–350 K suggests continuous rotation of Cr^{3+}, irreversibility in FCC and FCW below 30 K indicates the transformation of Cr^{3+} from one spin configuration to another. Such kind of irreversibility demonstrated in $SmCrO_3$ around T_{SR} confirms the polarization of spin configuration of Cr^{3+} from Γ_4 to Γ_2 below 30 K.[42] Although NPD analysis suggests the possibility of Γ_4 at high temperature and Γ_4 and/or Γ_2 at low temperature, the reversibility in M_{FCC} and M_{FCW} below 30 K rules out the Γ_4. Thus we confirm that the Γ_4 magnetic structure transitions to Γ_2 below 30 K in $CeCrO_3$.

2.3.2. Magnetization versus Field

Figure 7 depicts magnetization as a function of applied magnetic field (±7 T) measured at 5, 20, 40, 60, and 210 K in ZFC mode. At each temperature, M versus H shows a hysteresis loop with finite coercivity and remanent magnetization. Thus, we confirm that hysteresis is due to the spin canting of Cr^{3+} ions in $CeCrO_3$ like it is obvious in $GdCrO_3$, $TmCrO_3$, and $YbCrO_3$ materials.[35–37] It is further noticed that as the temperature decreases from 215 K

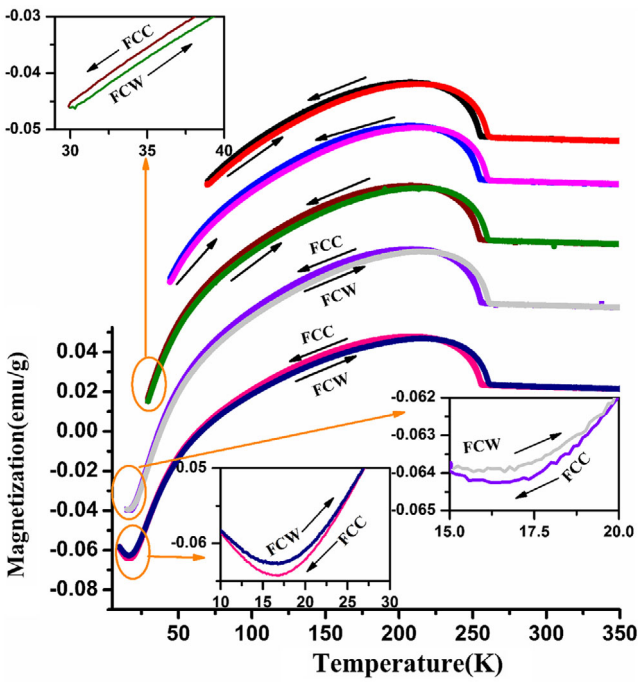

Figure 6. A sequence M versus T curves under 0.5 kOe field, in FCC and FCW mode, while turning back for FCW at decreasingly lower temperatures of 70, 45, 30, 15, and 10 K.

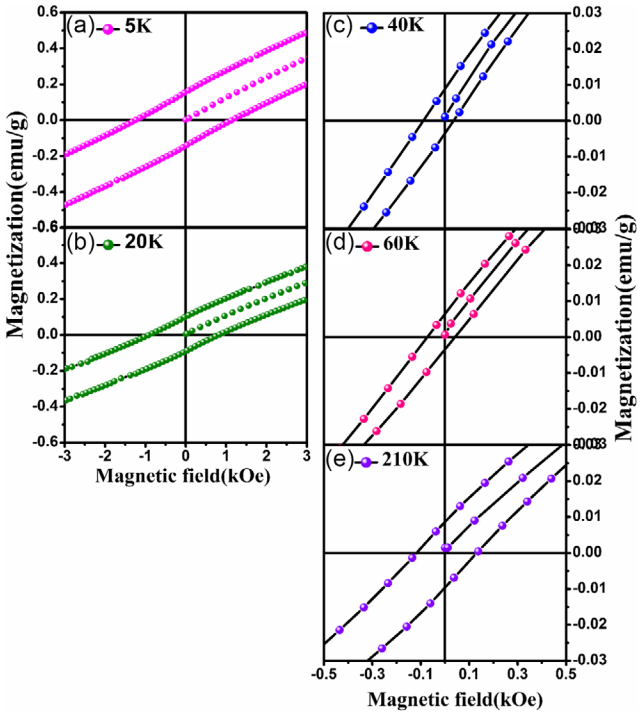

Figure 7. Isothermal magnetization curves, measured for $CeCrO_3$ in ZFC mode, at a–e) 5, 20, 40, 60, and 210 K, respectively.

(T_{max}) to 58 K (T_{comp}), coercivity declines followed by a saturation down to 40 K. Below 40 K, coercivity again increases showing a maximum at 5 K. In $RCrO_3$, four magnetic ground-state spin configurations such as Γ_1 (A_x, G_y, C_z), Γ_2 (F_x, C_y, G_z), Γ_3 (C_x, F_y, A_z), and Γ_4 (G_x, A_y, F_z) are allowed. The Γ_4 (G_x, A_y, F_z) remains weakly FM below T_N similar to the $LaCrO_3$ and $YCrO_3$ samples.[5] When R ion is nonmagnetic, the Γ_4 (G_x, A_y, F_z) persists throughout the temperature range of 2–300 K. When R is magnetic ion, not only Γ_4 (G_x, A_y, F_z) configuration but also Γ_1 (A_x, G_y, C_z) and Γ_2 (F_x, C_y, G_z) configurations are possible. Spin configuration, Γ_1 (A_x, G_y, C_z), does not allow any ferromagnetism and hence no hysteresis whereas Γ_2 (F_x, C_y, G_z) configuration shows a weak ferromagnetism along x direction and the presence of hysteresis.[14] It is also reported in $RCrO_3$ that coercivity for Γ_2 (F_x, C_y, G_z) spin configuration is higher compared to the Γ_4 (G_x, A_y, F_z) spin configuration.[14] As the coercivity at 5 K in $CeCrO_3$ nanoparticle is large compared to coercivity above T_{SR}, the possibility of transition from Γ_4 (G_x, A_y, F_z) to Γ_2 (F_x, C_y, G_z) through continuous rotation of Cr^{3+}could be expected. Further, the irreversibility in M_{FCC} and M_{FCW} from magnetization versus temperature measurement below T_{SR} supports the transition from Γ_4 to Γ_2. Hence we conclude that with decrease in temperature from 215 K, Γ_4 spin configuration is transformed to Γ_2 below T_{SR} in these nanoparticles. Further, to explore EB phenomena (H_E), M versus H is measured at different temperatures with a measuring field range of ±70 kOe under the field-cooling condition. Prior to each measurement, the sample is cooled down from 350 K to the desired temperature under a field of 10 kOe. Interestingly, a shift in FC MH is observed at 5 K, which indicates the presence of EB as shown in **Figure 8**. The exchange bias, H_E, is defined as $H_E = (H_1 + H_2)/2$, where H_1

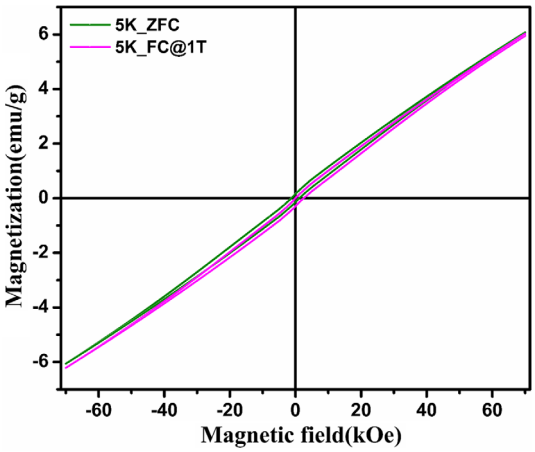

Figure 8. Isothermal magnetization curves, M versus H, measured for $CeCrO_3$ in ZFC and FC (@10 kOe) mode at 5 K.

and H_2 are the right and left coercivity fields in the M versus H curve. The field-cooled M versus H curves at various temperatures are shown in **Figure 9**. **Figure 10** depicts the temperature dependence of H_E. One may notice that NEB and PEB are observed at high temperature and at low temperature respectively. The highest PEB of 2.25 kOe is observed at around 40 K, while a minimum NEB of −1.25 kOe is detected at 210 K. Below 40 K, the exchange bias is decreased to 1.25 kOe at 5 K, whereas above 40 K, exchange bias decreases and shows minimum EB, −1.25 kOe at 210 K. It is clear from Figure 10 that

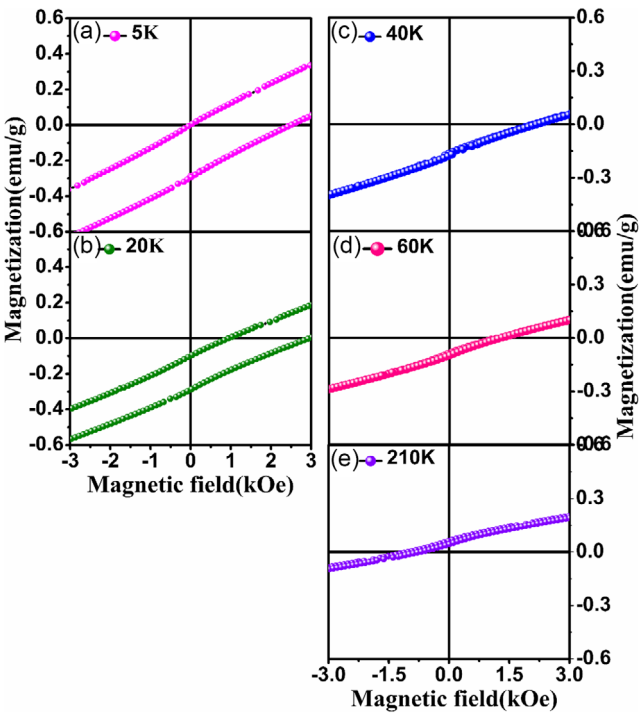

Figure 9. Isothermal magnetization curves, M versus H, measured for $CeCrO_3$ in FC (@10 kOe) mode at a–e) 5, 20, 40, 60, and 210 K, respectively.

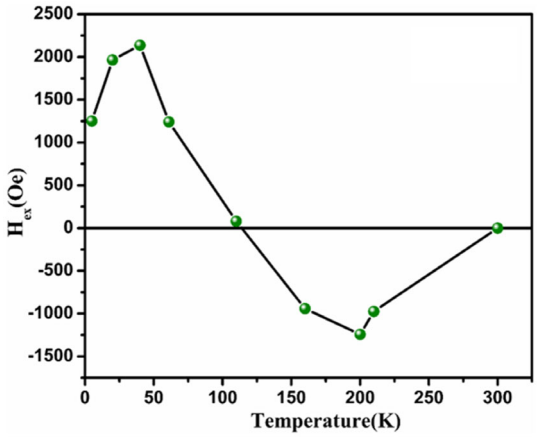

Figure 10. EB in 10 kOe FC *MH* at 5, 20, 40, 60, 110, 200, 210, and 300 K of $CeCrO_3$.

the EB undergoes a transition from positive to negative around T_{cross} (110 K). The switching behavior of the EB can be understood based on the AFM interaction between Cr^{3+} and Ce^{3+} ions in $CeCrO_3$. Above T_{cross}, although Cr^{3+} and Ce^{3+} moments are antiferromagnetically coupled, Cr^{3+} moments dominate over Ce^{3+}. During the demagnetization process, the AFM coupling hinders the reversal of Cr^{3+} moments and hence requires an additional field to bring the magnetization closer to zero. As a result, the hysteresis loop shifts in the negative direction along the H axis and shows NEB. Below T_{cross}, the influence of Ce^{3+} moments becomes more prominent, especially below T_{comp}. In this regime, the Ce^{3+} moments align with the external applied field and become parallel to the direction of Cr^{3+} moments as the field increases. Therefore, the AFM coupling between these moments supports the reversal of Ce^{3+} during the demagnetization process, leading to a smaller applied field in the negative direction required to achieve zero magnetization. Consequently, the hysteresis shifts in the positive direction along the field axis and shows PEB. A similar kind of switching of EB from positive to negative is also reported in $TmCrO_3$ and $YbCrO_3$.[36,37] The switching of PEB to NEB with varying temperature is suitable for thermally assisted magnetic memory devices.

3. Conclusion

The nuclear and magnetic structure of $CeCrO_3$ nanoparticle synthesized through solution combustion method was presented. While the temperature-dependent nuclear structure demonstrated no structural change from 6 to 300 K, magnetic structure analysis revealed the possible spin configurations such as Γ_4, Γ_2, and Γ_1 which could not be distinguished due to a small difference in lattice parameter between *a* and *c* and strong coupling of moment along *x* and *z* directions. *M* versus *T* measurement suggested the canted AFM ordering of Cr^{3+} in $CeCrO_3$ just below T_N. Besides, an irreversibility in M_{FCC} and M_{FCW} showed the transition of magnetic structure around T_{SR}. *M* versus *H* measurement showed a weak FM behavior with small H_C at 215 K which indicated Γ_4 (G_x, A_y, F_z) magnetic structure. However, below T_{SR} the ferromagnetism with increased H_C indicated the Γ_2 (F_x, C_y, G_z) spin structure. Hence, combining neutron diffraction with magnetization measurements confirmed the transition of magnetic structure from Γ_4 to Γ_2 in $CeCrO_3$ nanoparticles. Further, sign reversal of EB driven by temperature was also detected. The elucidating of PEB and NEB was observed due to the competition between the AFM coupling of M_{Cr} and M_{Ce}. Such behavior is the main principle to design a TAMRAM. Our new finding is expected to generate considerable interest among the researchers working on spintronics devices.

4. Experimental Section

Powder sample of $CeCrO_3$ was synthesized through solution combustion method using highly pure cerium nitrate, chromium nitrate, and glycine in stoichiometric ratio. The synthesis details were described in our previous reports.[39,40] The phase and crystal structure were characterized by conducting powder XRD measurements with Cu Kα (1.54 Å) radiation. Chemical composition and average particle size were obtained from SEM and EDS analysis using field-emission SEM (ZEISS SUPRA 40). Magnetization measurements were performed using a vibrating sample magnetometer option of Quantum Design Inc.'s Dynacool Physical Properties Measurement System. ZFC, FCC, and FCW magnetization measurements were carried out under various magnetic fields within the temperature range of 2–300 K. Magnetization versus magnetic field isotherms were performed at various temperatures, ranging from 5 to 300 K. Powder neutron diffraction were carried out in zero magnetic field at different temperatures between 6 and 300 K to determine its nuclear and magnetic structure. The TOF neutron diffraction was carried out at the powder diffractometer POGEN/BL-11A/SNS ($\lambda = 1.5$ Å), at Oak Ridge national laboratory, USA. All the neutron diffraction data were analyzed using Rietveld refinement Full-Prof suite program.

Acknowledgements

M.Y. expresses their gratitude to the Council of Scientific and Industrial Research (CSIR), New Delhi, India, for providing fellowship assistance. C.R. acknowledges the funding received under the Core Research grant (CRG/2020/000814) sponsored by SERB, India. The authors would like to acknowledge the Central Instrument Facility Center (CIFC) at the Indian Institute of Technology (Banaras Hindu University) for granting access to the SEM and Magnetic Property Measurement System (MPMS) facilities. Additionally, the authors extend their appreciation to Oak Ridge National Laboratory, Tennessee, USA, for their assistance with the neutron diffraction measurement.

Conflict of Interest

The authors declare no conflict of interest.

Data Availability Statement

The data that support the findings of this study are available from the corresponding author upon reasonable request.

Keywords

exchange biases, negative magnetizations, neutron diffractions, spin reorientations

Received: July 22, 2024
Revised: September 15, 2024
Published online: October 16, 2024

[1] T. Kimura, G. Lawes, T. Goto, Y. Tokura, A. P. Ramirez, *Phys. Rev. B: Condens. Matter Mater. Phys.* **2005**, *71*, 224425.
[2] T. Kimura, T. Goto, H. Shintani, K. Ishizaka, T. Arima, Y. Tokura, *Nature* **2003**, *426*, 55.
[3] Y. Tokunaga, S. Iguchi, T. Arima, Y. Tokura, *Phys. Rev. Lett.* **2008**, *101*, 097205.
[4] T. Yamaguchi, K. Tsushima, *Phys. Rev. B* **1973**, *8*, 5187.
[5] B. Rajeswaran, D. I. Khomskii, A. K. Zvezdin, C. N. R. Rao, A. Sundaresan, *Phys. Rev. B: Condens. Matter Mater. Phys.* **2012**, *86*, 214409.
[6] S. Mahana, U. Manju, P. Nandi, E. Welter, K. R. Priolkar, D. Topwal, *Phys. Rev. B* **2018**, *97*, 224107.
[7] S. Mahana, B. Rakshit, R. Basu, S. Dhara, B. Joseph, U. Manju, S. D. Mahanti, D. Topwal, *Phys. Rev. B* **2017**, *96*, 104106.
[8] R. White, *J. Appl. Phys.* **1969**, *40*, 1061.
[9] H. Horner, C. M. Varma, *Phys. Rev. Lett.* **1968**, *20*, 845.
[10] T. Yamaguchi, *J. Phys. Chem. Solids* **1974**, *35*, 479.
[11] K. Yoshii, *J. Solid State Chem.* **2001**, *159*, 204.
[12] K. Yoshii, *Mater. Res. Bull.* **2012**, *47*, 3243.
[13] H. J. Zhao, J. Íñiguez, X. M. Chen, L. Bellaiche, *Phys. Rev. B* **2016**, *93*, 014417.
[14] A. Durán, R. Escamilla, R. Escudero, F. Morales, E. Verdín, *Phys. Rev. Mater.* **2018**, *2*, 014409.
[15] S. Biswas, S. Pal, *Rev. Adv. Mater. Sci.* **2018**, *53*, 206.
[16] N. Kumar, A. Sundaresan, *Solid State Commun.* **2010**, *150*, 1162.
[17] A. Kumar, S. M. Yusuf, *Phys. Rep.* **2015**, *556*, 1.
[18] L. H. Yin, J. Yang, X. C. Kan, W. H. Song, J. M. Dai, Y. P. Sun, *J. Appl. Phys.* **2015**, *117*, 133901.
[19] Y. Cao, S. Cao, W. Ren, Z. Feng, S. Yuan, B. Kang, B. Lu, J. Zhang, *Appl. Phys. Lett.* **2014**, *104*, 232405.
[20] Y. K. Jeong, J.-H. Lee, S.-J. Ahn, H. M. Jang, *Solid State Commun.* **2012**, *152*, 1112.
[21] A. V. Kimel, B. A. Ivanov, R. V. Pisarev, P. A. Usachev, A. Kirilyuk, T. Rasing, *Nat. Phys.* **2009**, *5*, 727.
[22] M. Shao, S. Cao, S. Yuan, J. Shang, B. Kang, B. Lu, J. Zhang, *Appl. Phys. Lett.* **2012**, *100*, 222404.
[23] A. H. Cooke, D. M. Martin, M. R. Wells, *J. Phys. C: Solid State Phys.* **1974**, *7*, 3133.
[24] T. Moriya, *Phys. Rev.* **1960**, *120*, 91.
[25] N. Shamir, H. Shaked, S. Shtrikman, *Phys. Rev. B* **1981**, *24*, 6642.
[26] N. Sharma, B. K. Srivastava, A. Krishnamurthy, A. K. Nigam, *J. Alloys Compd.* **2012**, *545*, 50.
[27] S. I. Ohkoshi, Y. Abe, A. Fujishima, K. Hashimoto, *Phys. Rev. Lett.* **1999**, *82*, 1285.
[28] S. I. Ohkoshi, T. Iyoda, A. Fujishima, K. Hashimoto, *Phys. Rev. B* **1997**, *56*, 11642.
[29] H. Adachl, H. Ino, *Nature* **1999**, *401*, 148.
[30] W. H. Meiklejohn, C. P. Bean, *Phys. Rev.* **1957**, *105*, 904.
[31] J. Nogués, I. K. Schuller, *J. Magn. Magn. Mater.* **1999**, *192*, 203.
[32] E. F. Bertaut, J. Mareschal, *Solid State Commun.* **1967**, *5*, 93.
[33] E. F. Bertaut, *Acta Crystallogr., Sect. A* **1968**, *24*, 217.
[34] E. F. Bertaut, G. Bassi, G. Buisson, P. Burlet, J. Chappert, A. Delapalme, J. Mareschal, G. Roult, R. Aleonard, R. Pauthenet, J. P. Rebouillat, *J. Appl. Phys.* **1966**, *37*, 1038.
[35] M. Tripathi, T. Chatterji, H. E. Fischer, R. Raghunathan, S. Majumder, R. J. Choudhary, D. M. Phase, *Phys. Rev. B* **2019**, *99*, 014422.
[36] L. Wang, S. W. Wang, X. Zhang, L. L. Zhang, R. Yao, G. H. Rao, *J. Alloys Compd.* **2016**, *662*, 268.
[37] L. Wang, G. H. Rao, X. Zhang, L. L. Zhang, S. W. Wang, Q. R. Yao, *Ceram. Int.* **2016**, *42*, 10171.
[38] R. Shukla, A. K. Bera, S. M. Yusuf, S. K. Deshpande, A. K. Tyagi, W. Hermes, M. Eul, R. Pöttgen, *J. Phys. Chem. C* **2009**, *113*, 12663.
[39] M. Yadav, C. Rath, *J. Magn. Magn. Mater.* **2022**, *543*, 168610.
[40] M. Yadav, P. Tiwari, C. Rath, *J. Solid State Chem.* **2021**, *303*, 122537.
[41] M. Taheri, F. S. Razavi, Z. Yamani, R. Flacau, C. Ritter, S. Bette, R. K. Kremer, *Phys. Rev. B* **2019**, *99*, 054411.
[42] T. Sau, P. Yadav, S. Sharma, R. Raghunathan, P. Manuel, V. Petricek, U. P. Deshpande, N. P. Lalla, *Phys. Rev. B* **2021**, *103*, 144418.